Applied Catalysis B: Environmental 174 (2015) 403–412

Contents lists available at ScienceDirect

Applied Catalysis B: Environmental

journal homepage: www.elsevier.com/locate/apcatb

The prevalence of surface oxygen vacancies over the mobility of bulk oxygen in nanostructured ceria for the total toluene oxidation

Jose Manuel López[a], Alexander L. Gilbank[b], Tomás García[a,**], Benjamín Solsona[c,***], Said Agouram[d], Laura Torrente-Murciano[b,*]

[a] Instituto de Carboquímica (CSIC), C/Miguel Luesma 4, 50018 Zaragoza, Spain
[b] Department of Chemical Engineering, University of Bath, Bath BA2 7AY, UK
[c] Departament d'Enginyeria Química, Universitat de València, C/Dr. Moliner 50, 46100, Burjassot, Valencia, Spain
[d] Department of Applied Physics and Electromagnetism, Universitat de Valencia, C/Dr. Moliner 50, 46100 Burjassot, Valencia, Spain

ARTICLE INFO

Article history:
Received 19 December 2014
Received in revised form 13 February 2015
Accepted 11 March 2015
Available online 13 March 2015

Keywords:
Ceria
Nanotubes
Nanoparticles
Nanorods
Nanocubes
Nanostructures
Crystal size
Morphology
Toluene
Surface oxygen vacancies

ABSTRACT

This paper reveals the key importance of surface oxygen defects in the oxidation catalytic activity of nanostructured ceria. A series of nanostructured rods and cubes with different physico–chemical properties have been synthesized, characterized and tested in the total toluene oxidation. The variation of the temperature and base concentration during the hydrothermal syntheses of nanostructured ceria leads not only to different ceria morphologies with high shape purity, but also to structures with tuneable surface areas and defect concentrations. Ceria nanorods present a higher surface area and a higher concentration of bulk and surface defects than nanocubes associated with their exposed crystal planes, leading to high oxidation activities. However, for a given morphology, the catalytic activity for toluene oxidation is directly related to the concentration of surface oxygen defects and not the overall concentration of oxygen vacancies as previously believed.

1. Introduction

Ceria-based materials have been intensively studied in the catalysis field, either as pure dioxide (CeO_2) or doped materials, due to its high abundance and desirable combination of chemical and physical properties [1,2]. Especially, ceria-containing oxides have been researched and employed in a wide range of catalytic applications including the three-way catalytic system for exhaust gases [3], water gas shift reaction [4], VOC oxidation [5], steam reforming of alcohols [6], photocatalysis [7] and electrocatalysis [8] among others. In the recent years, research has focused on the understanding of the properties of nanostructured ceria as a way of tuning and further improving its redox activity, surface to volume ratio and oxygen storage capacity [9–12]. The catalytic activity of nanostructured ceria is strongly related to the exposed surface crystal plane. Computer modeling has shown that surface energy increases on the ceria surfaces from (1 1 1) plane to (1 1 0)<(1 0 0)<(2 1 0)<(3 1 0), the former one being the most stable. Sayle et al. [13] have shown that, theoretically, the (1 0 0) surface plane is catalytically more active than the (1 1 1) and (1 1 0) surfaces and Campbell and Esch [11,14] gave evidence of the surface oxygen vacancies on CeO_2 (1 1 1) being immobile at room temperature while clusters are formed at high temperatures. These theoretical predictions have been experimentally demonstrated in a series of studies. Mai et al. [9] have shown that ceria structures with (1 0 0)/(1 1 0) dominating planes present a higher activity toward the CO oxidation reaction due to their higher lattice oxygen migration from bulk to surface compared to the (1 1 1) dominated ceria. More recently, we have observed a similar trend for the full oxidation of volatile organic compounds [5] in accordance with the enhanced oxygen storage capacity of the (1 0 0) exposed surface [15].

Selective surface plane exposure can be successfully achieved by controlling the morphology of the material at the nanoscale.

* Corresponding author at: University of Bath, Claverton Down Road, BA2 7AY, Bath, UK. Tel. +44 1225 38 5857.
** Corresponding author. Tel.: +34 976 733977.
*** Corresponding author. Tel.: +34 963 544898.
E-mail addresses: tomas@icb.csic.es (T. García), benjamin.solsona@uv.es (B. Solsona), ltm20@bath.ac.uk (L. Torrente-Murciano).

http://dx.doi.org/10.1016/j.apcatb.2015.03.017

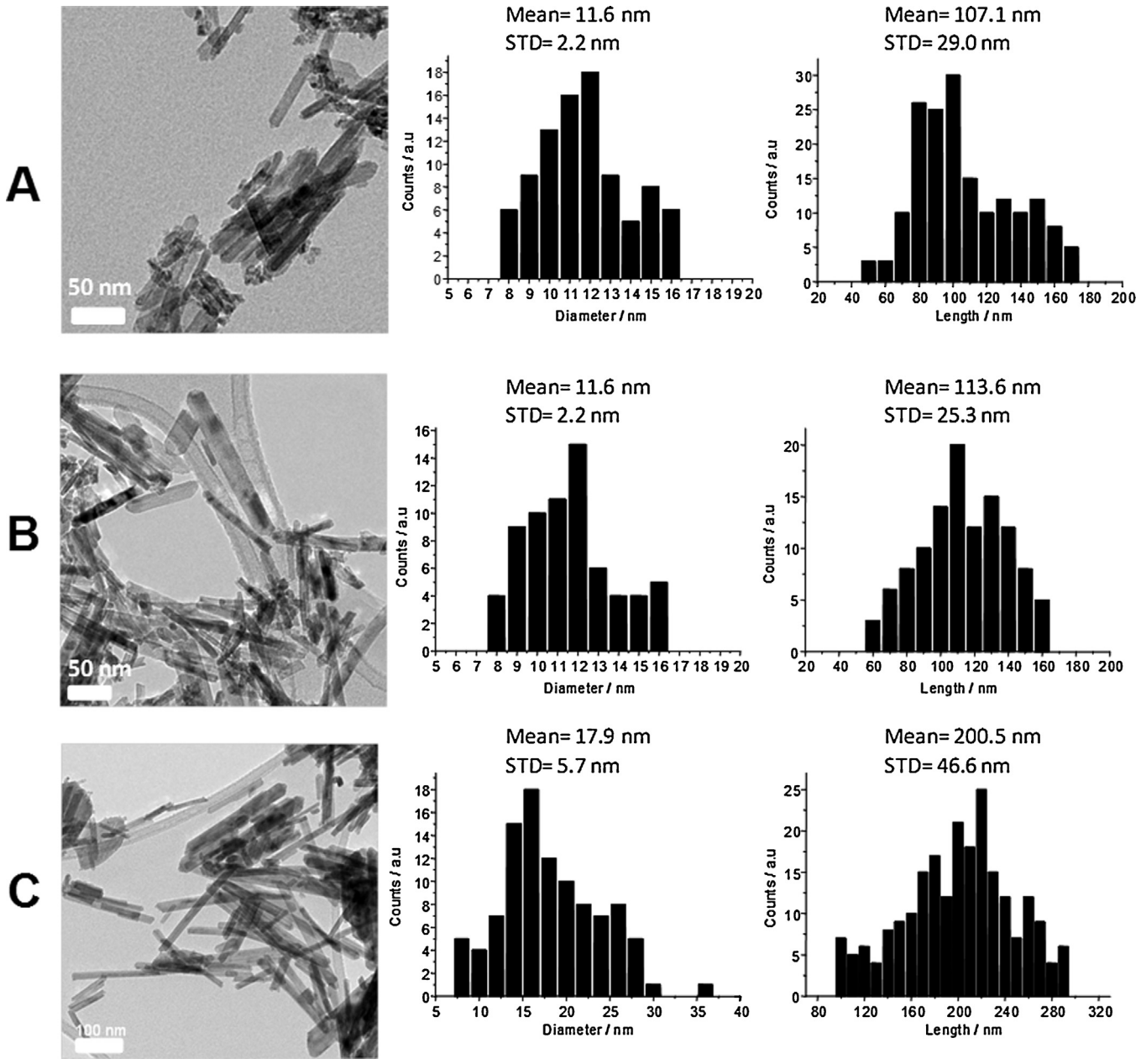

Fig. 1. TEM images and diameter and length histograms of ceria nanorods A). CeO_2_nr_A, B) CeO_2_nr_B and C) CeO_2_nr_C. A minimum of 200 rods were measured for each histogram.

Consequently, a variety of methods have been developed to synthesize nanosized ceria including the use of templates, special organic reagents, hydrothermal treatment, electrochemical methods, etc. [16,17] to form a wide range of morphologies from particles [10], polyhedrons [18], rods [19], tubes [20,21], spheres [6], cubes [22], etc.

Despite the importance of morphology in the final chemical and physical properties of ceria, particle and crystallite size are also believed to play a key role, especially determining its catalytic activity. However, this role is still not fully understood leading to the current debate in the literature. On the one hand, some studies show that the concentration of Ce^{3+} increases as the crystallite size decreases imparting unusual characteristics to the nano-sized material [22–24]. However, Xu et al. [10] claimed that the structural and chemical variations observed in ceria at sizes below 5 nm are due to the strain effect of higher surface energy associated with its lattice expansion with no relation to increasing the Ce^{3+} surface concentration. The oxygen storage capacity of the nanosized ceria seems to show a clear quantum effect [10], the smaller the particle size, the higher the observed reducibility, in terms of the utilization of surface oxygen [16]. It is important to highlight that particle size does not seem to be directly related to reducibility in zirconium-doped ceria [15]. However, most of these studies refer to particulated ceria and there is still a lack of understanding of the relative dependency of crystallite size and surface and bulk properties to catalytic activity of different ceria morphologies in which different surface planes are selectively exposed. In this paper, we show that crystallite size plays a key role in the reactivity of ceria rods with enclosing (1 1 0) and (1 0 0) facets, while it has the modest effect on the catalytic activity of ceria cubes with exposed (1 0 0) facets. More importantly, we demonstrate that the oxidation catalytic activity of nanostructured ceria shows a linear relationship with the concentration of surface oxygen defects playing a key role in the reaction mechanism, however, the concentration of

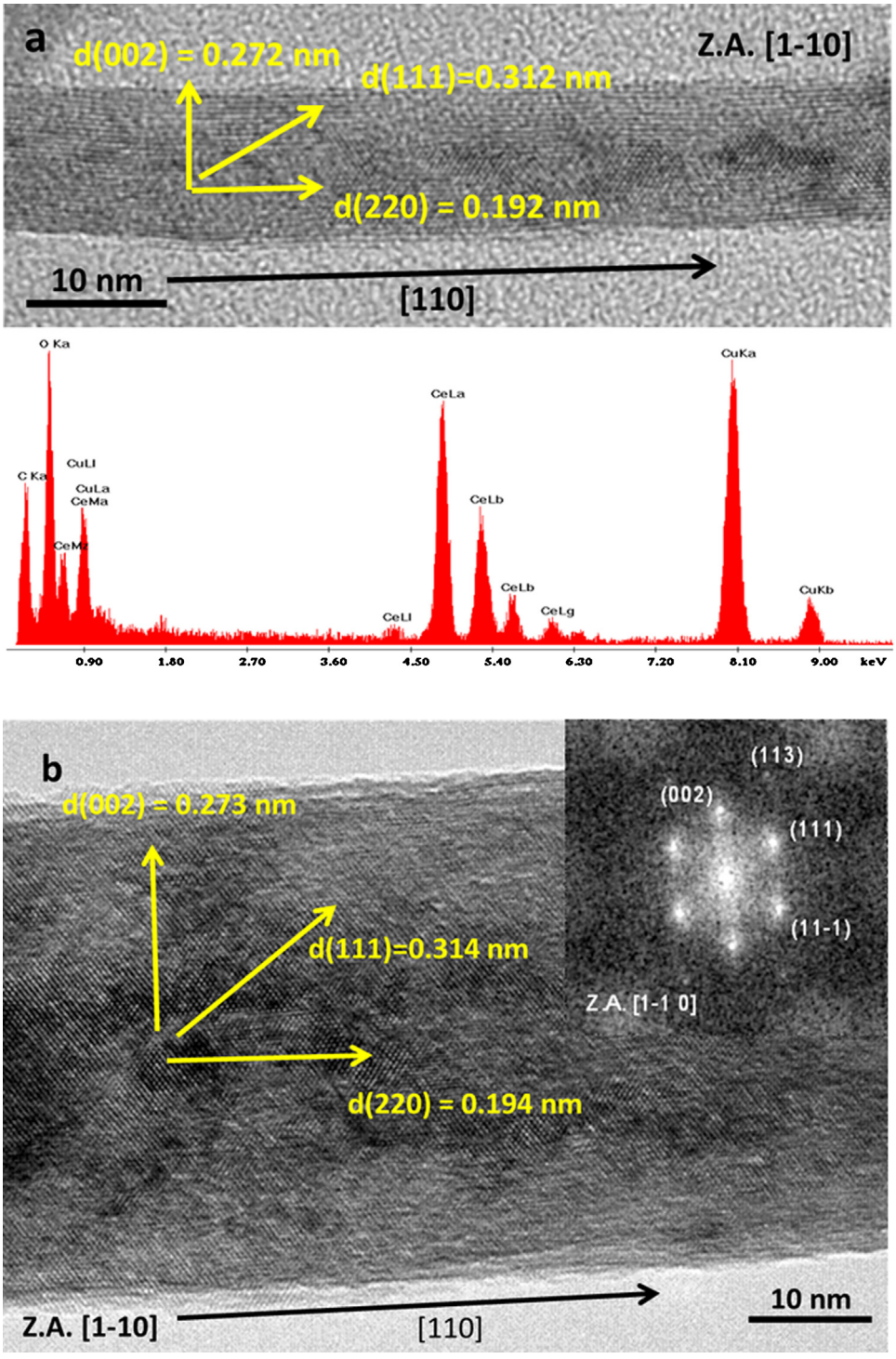

Fig. 2. HRTEM images (a) of a single nanorod of sample CeO_2_nr_A and its localised EDX analysis; (b) HRTEM images of a single nanorod of sample CeO_2_nr_C. Inset figure in HRTEM image is the digital electron diffraction pattern.

bulk oxygen defects is not directly related to the resulting catalytic activity.

2. Experimental

2.1. Synthesis and characterization of nanostructured ceria

Nanostructured ceria was synthesized by an alkali hydrothermal synthesis carried out inside an acid digestion bomb equipped with a 100 mL PTFE liner. 1.2 g of $Ce(NO_3)_3 \cdot 6H_2O$ was dissolved in 80 mL of NaOH of varying concentration between 5 and 15 M in deionised water [9]. The unstirred vessel was heated under autogenous pressure for 10 h inside an air-circulating oven to avoid temperature gradients. The synthesis conditions used for the different nanostructures are shown in Table 1.

After the reaction time, the autoclave reactor was allowed to cool to ambient temperature and the powder was filtered and washed with copious deionised water before being dried at 120 °C. Powder agglomerations were ground up to a fine powder using a pestle and mortar prior to characterization. Finally, the

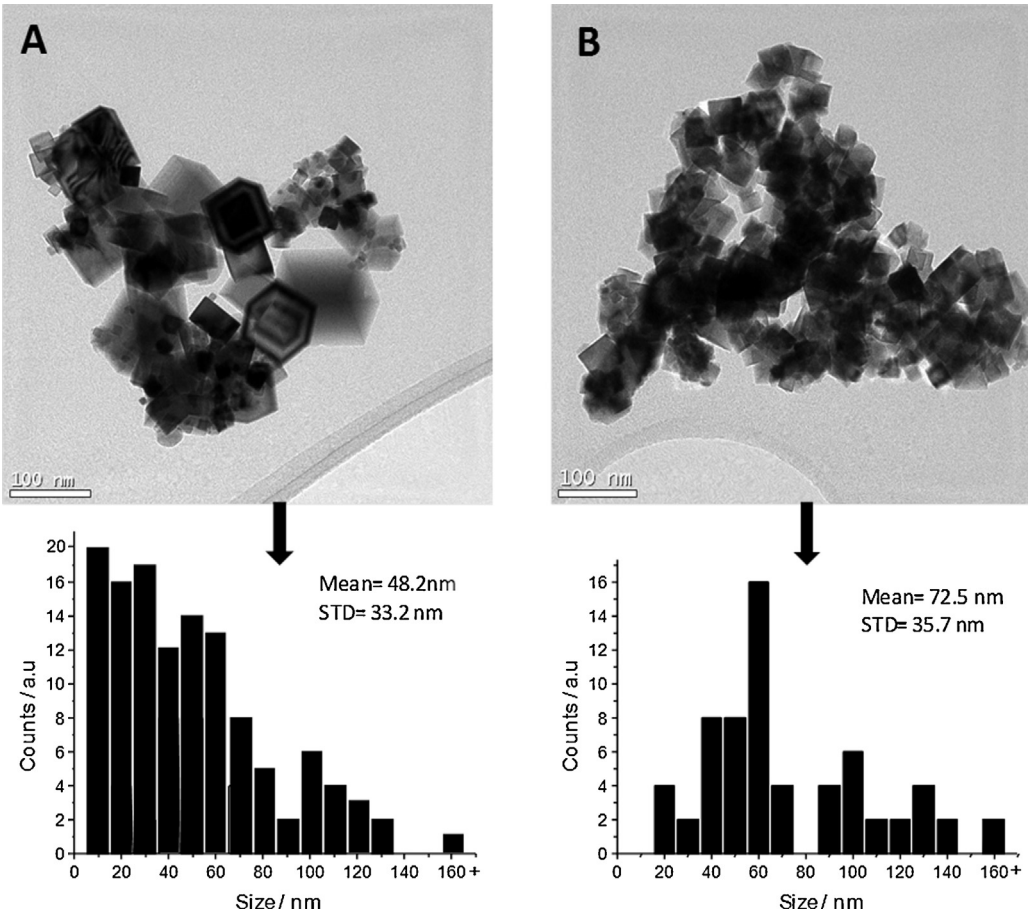

Fig. 3. TEM and diameter size distribution of ceria cubes A) CeO_2_nc_D and B) CeO_2_nc_E.

catalysts were calcined under 100 mL min^{-1} of synthetic air flow (80% N_2/20% O_2) at 400 °C for 4 h.

For comparative purposes ceria nanoparticles supplied by Sigma, pre-treated under the same conditions (calcination at 400 °C for 4 h) was also used.

Surface area was determined using low temperature nitrogen adsorption measurements at −156 °C on a Micromeritics ASAP 2020 apparatus. The specific surface area was calculated using the Brunauer–Emmett–Teller (BET) theory (associated error of ±0.5%). Transmission electron microscopy (TEM), high resolution TEM (HRTEM), selected area electron diffraction (SAED) and energy-dispersive X-rays spectroscopy spectral (EDX) was carried out using a Field Emission Gun (FEG) TECNAI G2 F20 microscope operated at 200 kV. X-ray diffraction (XRD) characterization was done using an X'Pert PRO diffractometer by PANalytical with a Cu Kα radiation and the crystalline phases were identified by matching the experimental patterns to the JCPDS powder diffraction file database. Temperature programed reductions (TPR) were carried out under a 50 mL min^{-1} 5% H_2/Ar flow from room temperature to 1000 °C with a heating rate of 10 °C min^{-1}. X-ray photoelectron spectroscopy (XPS) measurements were made on a Kratos Axis ultra DLD photoelectron spectrometer using a non-monochromatized Mg Kα X-ray source ($h\nu$ = 1253.6 eV). Analyzer pass energy of 50 eV was used for survey scans and 20 eV for detailed scans. Binding energies are referenced to the C1s peak from adventitious carbonaceous contamination, assumed to have a binding energy of 284.5 eV. XPS data were analyzed using CasaXPS software. All the peaks of the corrected spectra were fitted with a Gaussian–Lorentzian shape function to peak fit the data. Iterations were performed using the Marquardt method. Relative standard deviations were always lower than 1.5%. Unpolarised Raman spectra were obtained using a Renishaw system-1000 dispersive laser Raman microscope. The excitation source used was an argon green ion laser (532 nm) operated at a power of 20 mW and at room temperature. The laser was

Table 1
Physical properties of nanostructured CeO_2 catalysts.

Catalyst	Synthesis conditions		Predominant morphology	BET surface area/m^2 g^{-1}	Crystallite size[a]/nm
	[NaOH] /M	T /°C			
CeO_2_nr_A	15	70	Rods	98.4	6.4
CeO_2_nr_B	10	100	Rods	63.6	9.9
CeO_2_nr_C	15	100	Rods	53.6	14.6
CeO_2_nc_D	10	180	Cubes	5.2	37.3
CeO_2_nc_E	15	180	Cubes	6.7	35.2

[a] Mean value determined by XRD using the Williamson–Hall method.

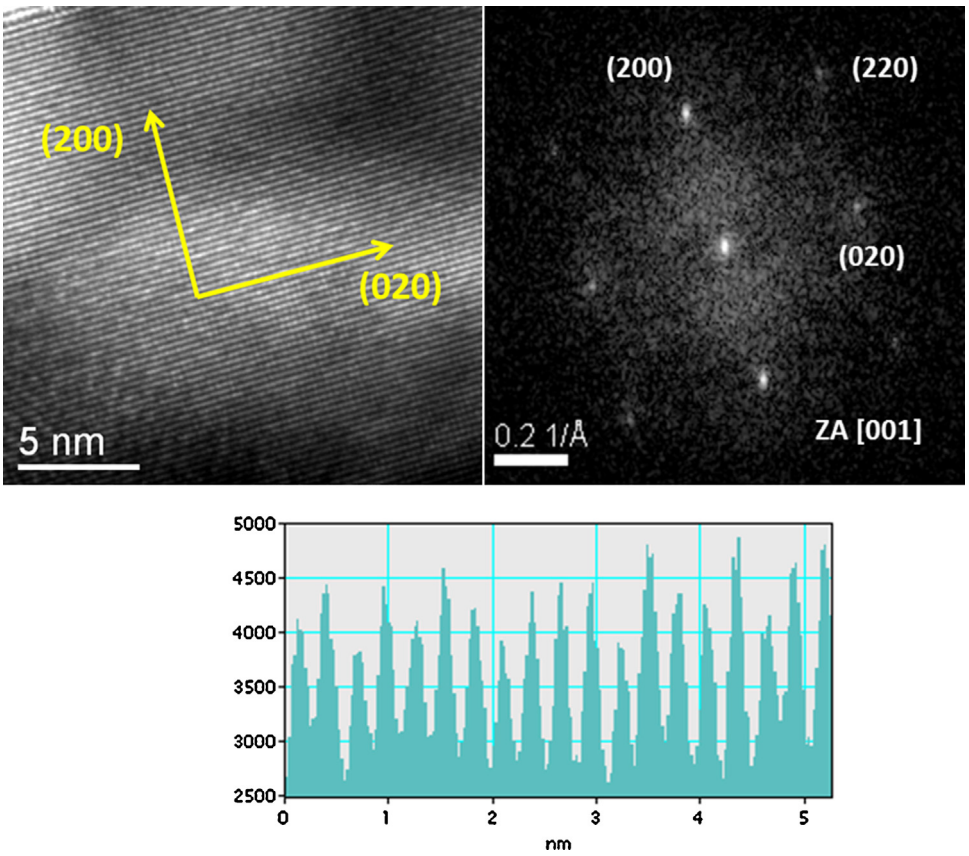

Fig. 4. HRTEM images of CeO_2_nr_D in [001] zone axis and its corresponding digital electron diffraction pattern and line profile along (200) direction.

focused on powdered samples placed on a microscope slide to produce a spot size ca. 3 μm in diameter. A backscattering geometry with an angle of 180° between illuminating and collected radiation was used for recording data. The acquisition time was 60 s for each spectrum with a spectral resolution of one cm^{-1}.

2.2. Toluene oxidation reactions

In each toluene oxidation test, 50 mg of nanostructured ceria powder (volume of ca. 115 mm^3) were loaded into a quartz microreactor (inner diameter 7 mm) operating under plug flow regime. The gas mixture consisted of 80 ppmv of toluene in synthetic air (20% of O_2 and Ar for balance). The total gas flow rate was fixed at 100 mL min^{-1}, with a gas hourly space velocity (GHSV) of 52000 h^{-1}. Experiments were conducted between 100 °C and 400 °C. The temperature was varied in 50 °C after which, steady state conditions were achieved prior gas analysis. The reaction feed and product were analyzed through gas chromatography using a TCD detector, with two columns for appropriate analysis (molecular sieve 5A and Porapak Q). Only CO_2 was obtained as product. The carbon balance was closed in all the experiments, with values of 100 ± 3%.

Additional experiments were conducted at 225 °C using the same gas mixture shown above but modifying the contact time in order to compare the reactivity of the different ceria catalysts synthesized with the aim of achieving appreciable catalytic activity but lower than 15%.

Blank tests in an empty reactor for toluene were conducted at the highest reaction temperature employed (400 °C) showing no conversion.

3. Results and discussion

Nanostructured ceria rods and cubes were synthesized by hydrothermal treatment. Variation of reaction temperature (between 70 and 180 °C) and base concentration (NaOH, from 10 to 15 M) results not only in different predominant morphologies, as previously shown by us with the establishment of a morphological

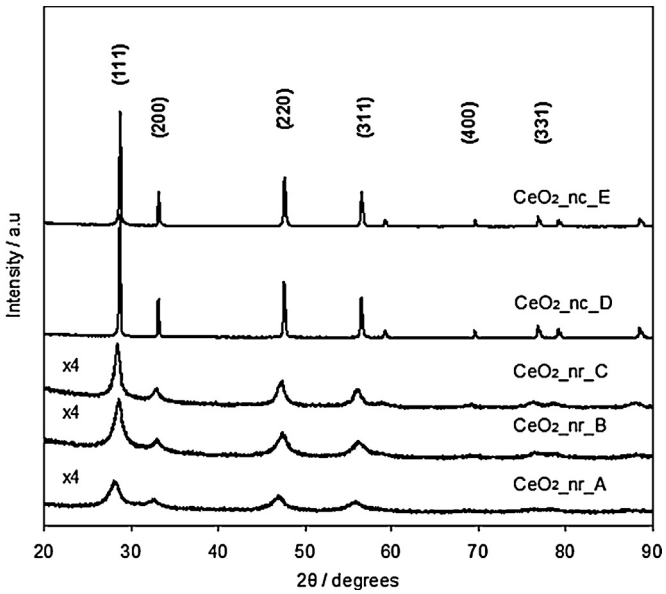

Fig. 5. XRD patterns of nanostructured ceria with different morphologies and crystallite size. Nomenclature and synthesis conditions given in Table 1.

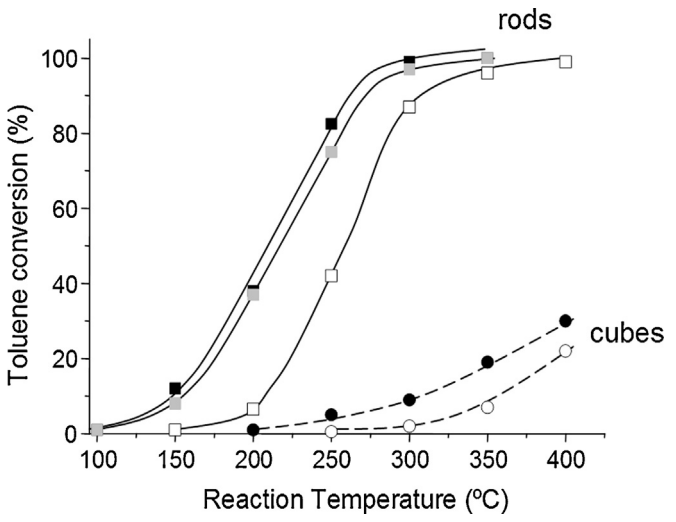

Fig. 6. Toluene oxidation conversion on nanostructured ceria as a function of reaction temperature. Nanorods: ■ CeO_2_nr_A, ■ CeO_2_nr_B, □ CeO_2_nr_C. Nanocubes: ● CeO_2_nr_D, ○ CeO_2_nr_E. Reaction conditions in text.

diagram [5], but also in different sizes and aspect ratios. Table 1 shows the predominant morphology and physical properties of the different nanostructured materials. Ceria nanorods with high morphological purity were synthesized by varying the hydrothermal treatment temperature between 70 and 100 °C and the base concentration between 10 and 15 M.

Fig. 1 shows representative TEM images of the three ceria nanorods materials. CeO_2_nr_A and CeO_2_nr_B rods present similar size distributions, where most of the rods have a length between 40 and 150 nm and diameters between 8 and 16 nm (mean diameter size is 11.6 nm in both cases). The mean length values are 107 and 114 nm for the CeO_2_nr_A and the CeO_2_nr_B respectively. As the hydrothermal base concentration is increased, a higher average length (201 nm) and diameter (17.9 nm) sizes are achieved in sample CeO_2_nr_C, with also broader distributions. The variation of the diameter size follows the expected trend with respect to temperature and base concentration during the synthesis in accordance with the well-known dissolution/recrystallization mechanism of nanostructured ceria [25,26]. A decrease in the diameter size of the nanorods implies an increase in their specific surface area ranging from 98.4 $m^2\ g^{-1}$ for the thinnest one to 53.6 $m^2\ g^{-1}$ for the thickest one (Table 1).

Fig. 2 shows HRTEM images of a single ceria nanorod of the CeO_2_nr_A and CeO_2_nr_C materials. CeO_2_nr_A shows the clear (1 1 1), (2 0 0), and (2 2 0), (3 1 1) and (2 2 2) lattice fringes with the interplanar spacing of 0.312, 0.272, and 0.192, 0.164 and 0.157 nm, respectively. In contrast, sample CeO_2_nr_C exhibits higher interplanar distances of about 0.314, 0.273 and 0.194 nm corresponding to (1 1 1), (2 0 0), and (2 2 0) lattice fringes, respectively, which are indexed as the cubic phase structure of cubic CeO_2 (JCPDS: 34-0394) with space group Fm3m. The electron diffraction pattern of the CeO_2_nr_C is shown in the inset of Fig. 2b, exhibiting at least five well-defined diffraction rings, characteristics of a polycrystalline nature of ceria powder. The concentric rings in the zero order Laue zone (ZOLZ) are produced by the ceria nanorods randomly dispersed providing a continuous angular distribution of (hkl) spots at a distance 1/dhkl from the (0 0 0) spot. The radius of the ring, r(hkl) and the interplanar lattice spacing, d(hkl), are related by $r(hkl) \times dhkl = L\lambda$, where $L\lambda = 1$, is the camera constant of the transmission electron microscope. From the electron diffraction pattern, r is measured and the lattice spacing is determined. No appreciable differences in the SAED patterns were found on samples CeO_2_nr_A, CeO_2_nr_B and CeO_2_nr_C. It is important to note that no obvious rings corresponding to metallic cerium or other cerium oxides compounds were observed in SAED patterns and the obtained cerium oxide nanorods are pure CeO_2 phase products. In agreement to this, the localized EDX spectrum of an individual ceria nanorod of sample CeO_2_nr_A is shown in Fig. 2a, where no significant amount of other elements were detectable apart from Ce (35.3% at.) and O (64.7% at.). The C and Cu peaks correspond to the Cu TEM grids. Similar EDX spectra were obtained on samples CeO_2_nr_B and CeO_2_nr_C, however, important differences between the different ceria nanorod samples were observed in terms of lattice parameter. Thus, the measured lattice parameter from interplanar distance of samples CeO_2_nr_A, CeO_2_nr_B and CeO_2_nr_C were 5.408, 5.413 and 5.438 Å, respectively. The lattice parameter values for samples CeO_2_nr_A and CeO_2_nr_B were comparable to the standard value (5.411 Å) of cubic CeO_2 JCPDS: 034-0394, whereas CeO_2_nr_C presented an expanded crystal structure.

Similarly, two ceria cube samples (CeO_2_nc_D and CeO_2_nc_E) were synthesized at the same hydrothermal temperature of 180 °C. Fig. 3 shows representative TEM images of the cubic ceria materials and their size distribution. The average size of the cubes increased from 48 to 72 nm as the base concentration increased from 10 to 15 M although in both case, a broad size distribution was observed. Apart from the different mean particle size, a remarkably different size distribution was observed between both cubic samples. In the

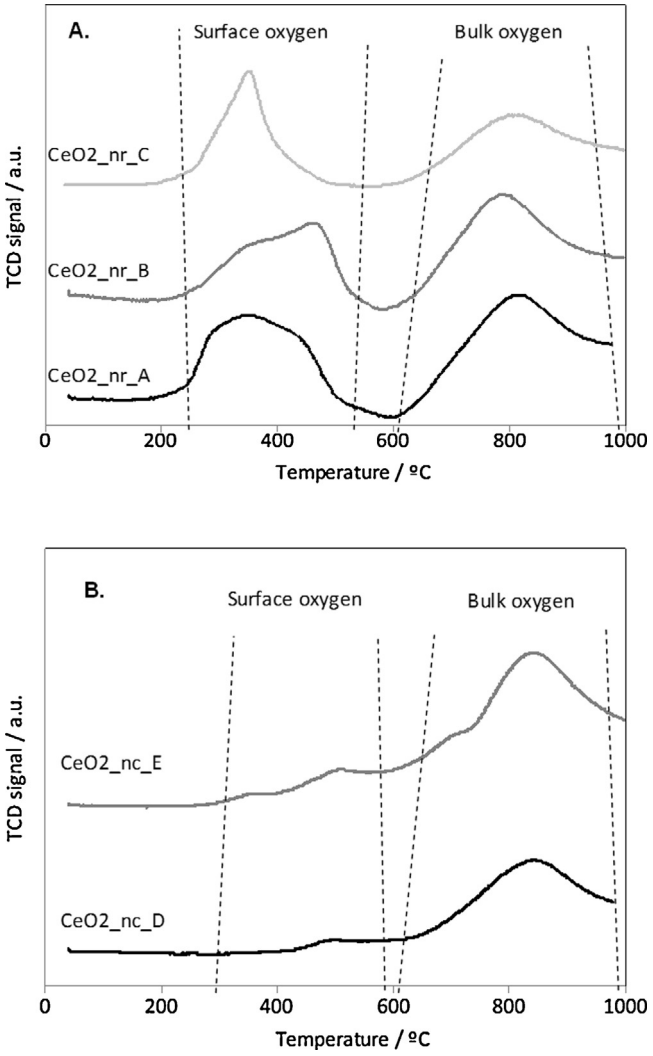

Fig. 7. Temperature program reduction of A. ceria nanorods and B. ceria nanocubes with different sizes.

CeO_2_nc_D sample, most of the cubes were 40 nm and smaller, but there were some large ones with sizes above 150 nm. However, the CeO_2_nc_E sample has a higher mean particle size, with most of the cubes have sizes between 40 and 70 nm, with few large particles. The specific surface areas for cubes present values c.a. 5–7 $m^2\ g^{-1}$ (Table 1). In both cases, a small amount of particulated material was observed surrounding the cubic structures, an intermediate stage of the previously mentioned dissolution/recrystallization mechanism [21].

The digital diffraction pattern and HRTEM image (Fig. 4) showed the monocrystalline quality of the CeO_2 cubes with the preferential exposure of the (1 0 0) crystal planes. The measured interplanar distances were found to be 0.27 nm and 0.19 nm corresponding to the (2 0 0) and (2 2 0) interplanar distance of the cubic phase structure of cubic CeO_2 (JCPDS: 34-0394) with space group Fm3m. Both cubic materials CeO_2_nc_D and CeO_2_nc_E show the same interplanar distances. According to the EDX results, sodium was not detected in any of the ceria materials (nanorod or nanocube).

All the samples, independently of their morphology, present a crystalline structure as shown by XRD (Fig. 5) with diffraction peaks at 2θ angles of 28.5°, 33.0°, 47.4°, 56.3°, 69.6° and 76.7° corresponding to the crystalline planes of the pure cubic phase (ceria fluorite structure, JCPDS 34-0394). The broadening of the reflections ascribed to the nanorods distinctly indicates their nanocrystalline nature, and the sharper reflections for nanocubes implied their larger sizes. Nanorod samples A and B present the smallest crystallite size calculated using the Williamson–Hall method (6.4 and 9.9 nm) followed by sample C that shows a higher crystallite size (14.6 nm). On the other hand, nanocube samples present the largest crystallite size (over 35 nm). These values obtained by XRD are lower but follow the same trend that the mean crystallite sizes determined by TEM.

Toluene oxidation reaction was used to assess the catalytic oxidation activity of the different nanostructured ceria materials (Fig. 6). Generally, ceria nanorods present an activity (mol toluene $kg_{catal}^{-1}\ h^{-1}$) of an order of magnitude higher than ceria nanocubes. Additionally, and relevant for industrial applications, ceria nanorods present activity for toluene full oxidation at temperature as low as 125 °C while ceria cubes can only oxidize toluene at temperatures above ca. 250 °C.

Despite the difference in activity among the ceria rods, the similarity in the minimum temperature of activity suggests the presence of similar active sites among the tubular materials. A similar observation applies to the ceria cubes. As expected, the catalytic activity increases as the surface area increases and as the crystallite size decreases, being the ceria rods materials more active than the cubes counterparts. Focusing on the oxidation activity of different ceria nanorods at 200 °C, it can be observed that the catalyst with the highest surface area (CeO_2_nr_A), presents the highest reaction rate followed by CeO_2_nr_B and finally CeO_2_nr_C, with the lowest surface area and consequently, activity. However, normalization of the catalytic activity per unit of surface area (mol toluene $m^{-2}\ h^{-1}$) reveals the importance of other physical properties on the determination of the intrinsic catalytic activity (Table 2).

While CeO_2_nr_C presents the lowest specific activity per surface area among the different ceria rods, the difference in activity between CeO_2_nr_A and CeO_2_nr_B cannot be ascribed only to the variations in surface area. Moreover, for a given reaction temperature (e.g., 225 °C), the toluene conversion achieved for the ceria rods is two orders of magnitude higher than that achieved with ceria nanocubes, while the difference in surface area between both morphologies is only one order of magnitude higher. Ceria nanorods are remarkably more active than ceria nanocubes and the difference is not only the result of the higher surface area.

To further investigate the cause of this variation in activity, the three nanorod samples were characterized by temperature programme reduction (TPR) up to 1000 °C to quantify their oxygen storage capacity potential as shown in Fig. 7A. The first broad peak starting at ~250 °C is related to the reduction of the readily reduced ceria oxygen while the second one at ~620 °C corresponds to bulk oxygen [10]. Highly reducible oxygen is more readily available and as such reduces at a lower temperature than the ceria bulk oxygen. At 1000 °C, almost all of the ceria is fully reduced to Ce_2O_3. Independently of the different diameter sizes, the three nanorod samples present a similar proportion of surface (ca. 40%) and bulk ceria (ca. 60%), as shown in Table 2. However, close inspection of the TPR profiles suggested the presence of different forms of surface oxygen present in the ceria nanorod surfaces, likely due to the presence of OH and carbonate species as discussed below. Consequently, the increase in oxidation catalytic activity as the crystallite size is decreased cannot be directly related to the concentration of highly reducible oxygen detected by TPR.

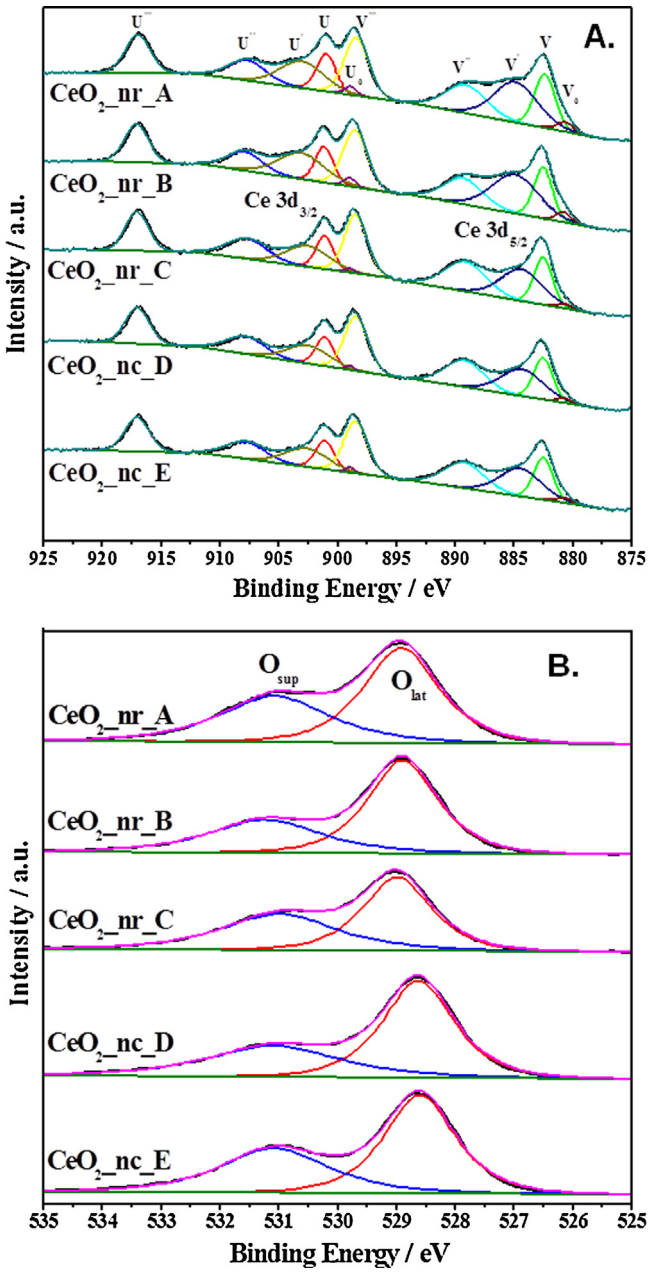

Fig. 8. XPS spectra for nanostructured ceria with different morphologies: (A) Ce3d spectra and (B) O1s spectra. Nomenclature and synthesis conditions given in Table 1.

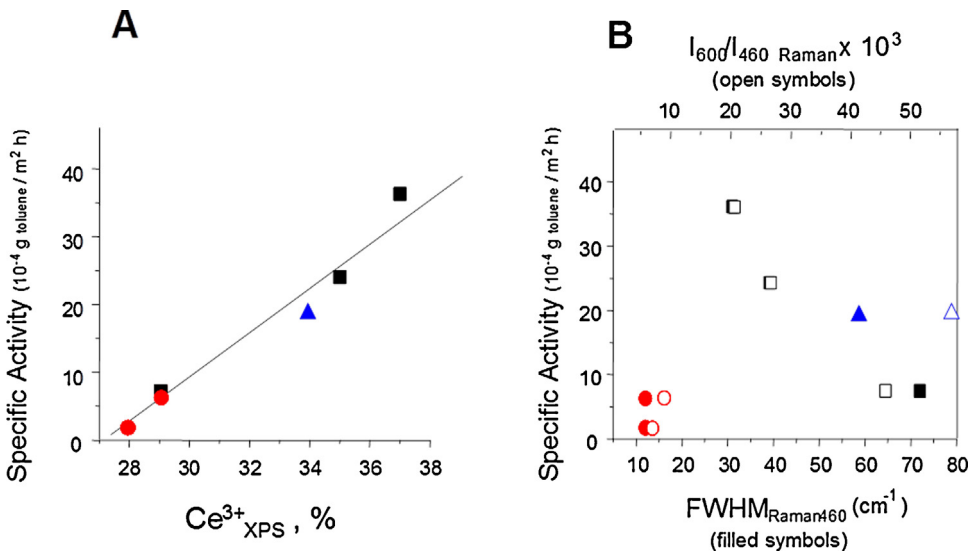

Fig. 9. Influence of the oxygen defects on the catalytic performance of ceria nanorods. (A) Specific rate vs $Ce^{3+}/(Ce^{3+}+Ce^{4+})$ determined by XPS and (B) Specific rate vs $FWHM_{460}$ Raman and I_{600}/I_{460}. Symbols: (●,○) cubes, (■,□) rods, nanoparticles from Sigma (▲). Reaction conditions in text. Reaction rates at 225 °C.

In contrast to ceria nanorods, almost no readily reducible oxygen is present in any of the nanocube samples as suggested by the very small reduction peaks starting at ca. 450 °C in Fig. 7B. Only 10% of the oxygen reduced in the TPR is readily reducible oxygen, whereas most of the cubic materials are reduced at temperatures above 700 °C, corresponding to bulk ceria oxygen [10].

X-ray photoelectron spectroscopy characterization of the different nanostructured ceria was carried out to provide information about the oxidation state of cerium and the nature of the O species. It is important to notice that XPS is a surface analysis technique with a sampling volume that extends from the surface to a depth of only ~50–70 Å. The interpretation of the XPS spectra of Ce3d, shown in Fig. 8A, is highly complex with overlapped peaks, however, according to previous published methods [5,27,28] an accurate deconvolution can be made. The analysis revealed two principal signals at binding energies about 882.5 and 901.1 eV corresponding to Ce $3d_{5/2}$ and Ce $3d_{3/2}$ respectively. These two peaks and four additional satellite peaks at 889.2, 898.5, 907.8 and 917.1 eV associated with their ionization processes are characteristic of Ce^{4+}, whilst peaks at 880.7, 884.4, 898.8 and 902.6 eV are characteristic of Ce^{3+}.

The amount of reduced, non-stoichiometric cerium (Ce^{3+}) in each of the samples is quantified in Table 2. In general, the toluene oxidation intrinsic catalytic activity of the nanostructured ceria increases as the amount of Ce^{3+} increases, as the presence of Ce^{3+} ions implies the formation on the surface of non-stoichiometric CeO_2. Ce^{3+} ions associated with the presence of oxygen vacancies play a critical role in the oxidation mechanism participating in both the activation of toluene (surface oxygen vacancies) and migration of oxygen toward the surface material (sub-surface oxygen vacancies) [24]. The ratio between both types of oxygen vacancies is determined by the exposed surface planes. While the (1 0 0) plane, present in both rods and cubes morphologies, is cerium terminated with almost no surface oxygen vacancies in its surface (except in defects such as corners or steps), a high proportion of surface oxygen vacancies is expected in the partially reduced (1 1 0) plane, present in the rod morphology, which is oxygen terminated. Taking these crystallographic aspects into consideration the oxidation catalytic activity was plotted vs the concentration of surface Ce^{3+} (Fig. 9A). It must be noted that as the reactivity of nanocubes and nanorods is very different, a proper comparison of catalytic activity at a fixed reaction temperature is not straightforward with a simple light-off curve. For this reason, we conducted new catalytic experiments fixing a reaction temperature in 225 °C and using different residence times in the reactor depending on the catalyst tested, with the objective of achieving conversions between 5 to 20% in all cases. Therefore, for nanocubes, high catalyst loadings were used and low loadings for nanorods. Thus, a clear relationship between the concentration of Ce^{3+} and oxidation catalytic activity was observed regardless of the structure of the ceria catalysts tested (rods or cube). Ceria nanoparticles supplied by Sigma were also tested for toluene oxidation to validate this relationship. Positively, it was seen that this catalyst fits well with the previous observed trend in Fig. 9A. A similar relationship has been previously observed with particulated ceria [25,29].

The O1s XPS spectra are shown in Fig. 8B where two different bands are mainly observed, the first band at 529.0 eV (called Oα) and the second band at 531 eV (called Oβ). Oα is commonly

Table 2
Characterization of nanostructured ceria and their catalytic activity in the oxidation of toluene.

Catalyst	TPR		XPS			Raman		Activity at 225 °C	
	Surface (O) %	Bulk (O) %	Ce^{3+} (at.%)	Oα (at.%)	Oβ (at.%)	$FWHM_{460}$ (cm^{-1})	I_{600}/I_{460}	$g_{toluene}$ $kg_{catal}^{-1}h^{-1}$	$g_{toluene}$ m^{-2} h^{-1} × 10^4
Nanorods									
CeO_2_nr_A	40.4	59.6	35	59	41	39	0.026	23.4	23.8
CeO_2_nr_B	37.2	62.8	37	63	37	31	0.021	22.6	35.7
CeO_2_nr_C	41.6	58.4	29	54	46	72	0.045	3.71	6.9
Nanocubes									
CeO_2_nc_D	7.0	93.0	29	62	38	12	0.007	0.32	6.1
CeO_2_nc_E	13.5	86.5	28	59	41	12	0.009	0.077	1.5

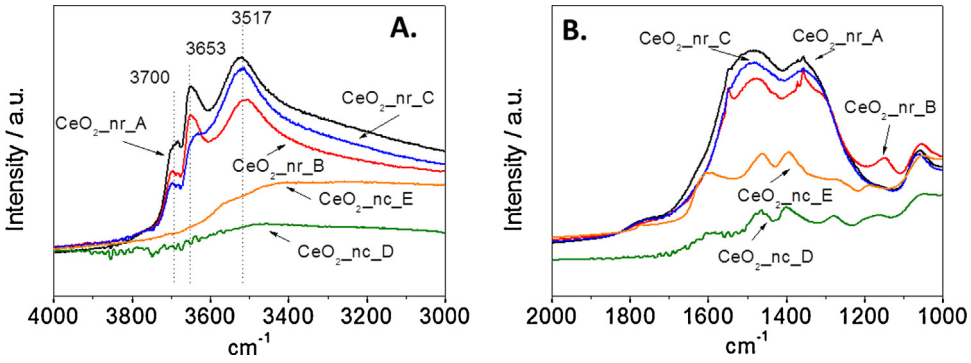

Fig. 10. DRIFTS spectra of ceria nanorods and nanocubes

associated with lattice oxygen whilst Oβ with oxygen vacancies. However, the latter can should also be associated with surface adsorbed oxygen, hydroxyl groups and carbonates [30]. This fact could explain the lack of correlation found in this work between the relative contribution of this band and the number of oxygen vacancies. DRIFTS studies were carried out to get further information of the OH and carbonate species present in the different nanostructured ceria surfaces, probing that the contribution of these species strongly diverges for these samples. The DRIFTS spectra corresponding to the OH region of the dehydrated ceria catalysts are shown in Fig. 10A after in-situ treatment with synthetic air at 150 °C. The spectra of the ceria nanorods (CeO2_nr_A, CeO2_nr_B and CeO2_nr_C) presented three bands in the OH vibrational region. The band peak at 3700 cm^{-1} was assigned to mono-coordinated OH (type I); the band at 3653 cm^{-1} was assigned to bridging OH (types II); and a broad band centered at 3517 cm^{-1} was assigned to triply bridging OH (III) species [31]. Although similar hydroxyl species are present on the ceria nanorod surfaces, significant differences on the relative intensities of these band peaks can be observed.

It should be pointed out that mono and bridging coordinated hydroxyl groups are clearly more apparent for CeO2_nr_A and CeO2_nr_B, which are those samples with the highest surface area. Therefore, it could be tentatively proposed that the these OH sites could act as adsorption points in the first reaction step at low temperature, in the agreement with the results previously published for naphthalene oxidation [31]. Conversely, the intensity of the OH species bands is negligible in the CeO2 nanocube samples, what could also be related to the low activity of these samples at low temperature.

On the other hand, although the assignment of stretching vibration modes of the O—C—O group of carbonate species is complicated, and their detailed analysis is beyond the scope of this manuscript, it can be observed that all nanostructured ceria, both rods and cubes, presented broad bands in this region (Fig. 10B), which can be tentatively assigned to different types of surface carbonate and carboxylate groups [32].

The Raman spectra for all the nanostructured ceria catalysts are shown in Fig. 11. Two main peaks can be observed, the peak centered around 460 cm^{-1} is characteristic of the CeO_2 vibrations (the triply degenerated TO mode) [33], whilst the broad peak at around 600 cm^{-1} (see Fig. 11 insets) is characteristic of the defect induced (D) mode associated with the presence of oxygen vacancies due to the existence of Ce^{3+} ions [29]. The intensity ratio of these two peaks, I_{600}/I_{460}, represents the relative oxygen vacancy concentration (Table 2). Additionally, the full width at half maximum of the main peak at 460 cm^{-1} ($FWHM_{460}$) is affected by both the crystallite size and the amount of oxygen vacancies [23,24]. Thus, a high FWHM value is associated with a low crystallite size and/or a high amount of oxygen vacancies in the CeO_2 structure. The ceria nanorods CeO_2_nc_C present by far the highest I_{600}/I_{460} ratio and the highest FWHM value among all the ceria nanorods materials. However, XRD and TEM characterization shows that the CeO_2_nc_C material has the bigger average size and crystallite size which suggest that the high I_{600}/I_{460} ratio and FWHM values are mainly associated with a high concentration of oxygen vacancies in the material. The discrepancies of the concentration of oxygen vacancies within the ceria nanorods materials estimated by XPS and Raman spectroscopy is associated with the characterization volume of both techniques, the former being more superficial than

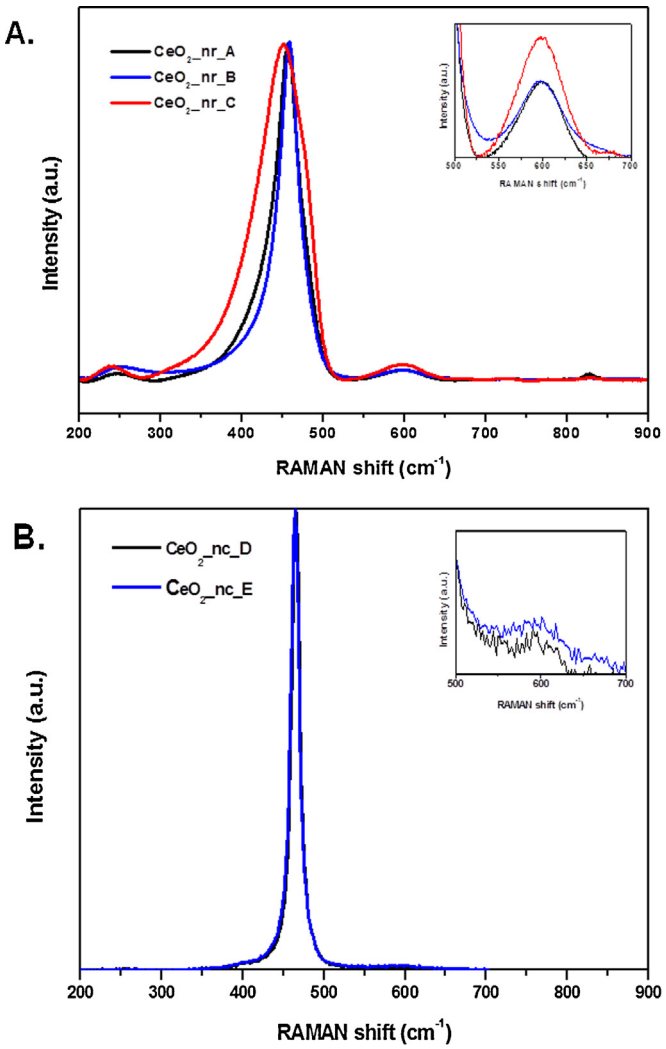

Fig. 11. Raman spectra for nanostructured ceria with different morphologies: (A) nanorods (B) nanocubes.

the latter. In this way, it can be concluded that the specific oxidation catalytic activity of the ceria nanorods is directly related to the concentration of surface oxygen vacancies involved in the toluene activation, rather than the concentration of bulk oxygen vacancies involved in the migration of oxygen to the surface during the catalytic cycle [1] as can be observed in Fig. 9B. Thus, the relationship between concentration of bulk oxygen vacancies, estimated by I_{600}/I_{460} ratio and the FWHM, with the catalytic activity follows an erratic trend. All this observations suggest that the most important step in the toluene oxidation is the adsorption/chemisorption of toluene on the surface of the catalyst rather than the migration of oxygen species from bulk and the further oxidation. Additional investigations are needed to elucidate whether these observations are reaction-dependant or whether they are applicable to other oxidation reactions (e.g., CO oxidation).

Finally, it is important to highlight that ceria nanorods not only present a high activity, activating toluene at temperatures ~125 °C but this nanostructured material also presents a high stability at higher temperatures (250 °C), maintaining its activity under reaction conditions for at least 48 h.

4. Conclusions

Modifications to the synthetic route of nanostructured ceria leads to a variation of ceria nanorods and nanocubes with different physicochemical properties, mainly surface area, crystallite size, surface reducibility (presence of Ce^{3+}) and concentration of surface vacancies. Among them, the concentration of surface defects and the exposed crystal surface planes play a key role in the toluene oxidation catalytic activity. Interestingly, it has been observed that for this oxidation system, the catalytic activity does not show a direct relationship with the amount of bulk/sub-surface defects as suggested previously in the literature.

Acknowledgments

The authors would like to acknowledge the UK Engineering and Physical Science Research Council (grant number EP/K016334/1 and EP/L020432/1) for funding, the University of Bath for ALG's studentship and the Research Catalysis Group at Harwell (RCaH) for access to the TEM microscopy facilities. B.S. would like to thank the DGICYT in Spain (CTQ2012-37925-C03-2) for financial support. J.M. López would also like to thank Spanish MICINN and CSIC for founding his Ramon y Cajal contract (RYC-2009-04483).

References

[1] C.W. Sun, H. Li, L.Q. Chen, Nanostructured ceria-based materials: synthesis, properties, and applications, Energy Environ. Sci. 5 (2012) 8475–8505.
[2] M. Mogensen, N.M. Sammes, G.A. Tompsett, Physical, chemical and electrochemical properties of pure and doped ceria, Solid State Ion 129 (2000) 63–94.
[3] J. Kaspar, P. Fornasiero, M. Graziani, Use of CeO_2-based oxides in the three-way catalysis, Catal. Today 50 (1999) 285–298.
[4] F.R. Garcia-Garcia, L. Torrente-Murciano, D. Chadwick, K. Li, Hollow fibre membrane reactors for high H-2 yields in the WGS reaction, J. Membr. Sci. 405 (2012) 30–37.
[5] L. Torrente-Murciano, A. Gilbank, B. Puertolas, T. Garcia, B. Solsona, D. Chadwick, Shape-dependency activity of nanostructured CeO_2 in the total oxidation of polycyclic aromatic hydrocarbons, Appl. Catal. B: Environ. 132–133 (2013) 116–122.
[6] C.W. Sun, J. Sun, G.L. Xiao, H.R. Zhang, X.P. Qiu, H. Li, L.Q. Chen, Mesoscale organization of nearly monodisperse flowerlike ceria microspheres, J. Phys. Chem. B 110 (2006) 13445–13452.
[7] S. Kundu, J. Ciston, S.D. Senanayake, D.A. Arena, E. Fujita, D. Stacchiola, L. Barrio, R.M. Navarro, J.L.G. Fierro, J.A. Rodriguez, Exploring the structural and electronic properties of Pt/ceria-modified TiO2 and its photocatalytic activity for water splitting under visible light, J. Phys. Chem. C 116 (2012) 14062–14070.
[8] W. Lai, S.M. Haile, Impedance spectroscopy as a tool for chemical and electrochemical analysis of mixed conductors: a case study of ceria, J. Am. Ceram. Soc. 88 (2005) 2979–2997.
[9] H.X. Mai, L.D. Sun, Y.W. Zhang, R. Si, W. Feng, H.P. Zhang, H.C. Liu, C.H. Yan, Shape-selective synthesis and oxygen storage behavior of ceria nanopolyhedra, nanorods, and nanocubes, J. Phys. Chem. B 109 (2005) 24380–24385.
[10] J.H. Xu, J. Harmer, G.Q. Li, T. Chapman, P. Collier, S. Longworth, S.C. Tsang, Size dependent oxygen buffering capacity of ceria nanocrystals, Chem. Commun. 46 (2010) 1887–1889.
[11] C.T. Campbell, C.H.F. Peden, Chemistry – oxygen vacancies and catalysis on ceria surfaces, Science 309 (2005) 713–714.
[12] D.Y. Wang, Y.J. Kang, V. Doan-Nguyen, J. Chen, R. Kungas, N.L. Wieder, K. Bakhmutsky, R.J. Gorte, C.B. Murray, Synthesis and oxygen storage capacity of two-dimensional ceria nanocrystals, Angew. Chem. Int. Ed. 50 (2011) 4378–4381.
[13] D.C. Sayle, S.A. Maicaneanu, G.W. Watson, Atomistic models for CeO_2(1 1 1), (1 1 0), and (1 0 0) nanoparticles, supported on yttrium-stabilized zirconia, J. Am. Chem. Soc. 124 (2002) 11429–11439.
[14] F. Esch, S. Fabris, L. Zhou, T. Montini, C. Africh, P. Fornasiero, G. Comelli, R. Rosei, Electron localization determines defect formation on ceria substrates, Science 309 (2005) 752–755.
[15] R.G. Wang, M.H. Fang, Improved low-temperature reducibility in ceria zirconia nanoparticles by redox treatment, J. Mater. Chem. 22 (2012) 1770–1773.
[16] P. Singh, M.S. Hegde, Controlled synthesis of nanocrystalline CeO(2) and Ce(1 − x)M(x)O(2-delta) (M = Zr, Y, Ti, Pr and Fe) solid solutions by the hydrothermal method: structure and oxygen storage capacity, J. Solid State Chem. 181 (2008) 3248–3256.
[17] D. Tsukamoto, M. Ikeda, Y. Shiraishi, T. Hara, N. Ichikuni, S. Tanaka, T. Hirai, Selective photocatalytic oxidation of alcohols to aldehydes in water by TiO_2 partially coated with WO_3, Chem. Eur. J. 17 (2011) 9816–9824.
[18] L. Yan, R.B. Yu, J. Chen, X.R. Xing, Template-free hydrothermal synthesis of CeO_2 nano-octahedrons and nanorods: investigation of the morpholog evolution, Cryst. Growth Des. 8 (2008) 1474–1477.
[19] K.B. Zhou, X. Wang, X.M. Sun, Q. Peng, Y.D. Li, Enhanced catalytic activity of ceria nanorods from well-defined reactive crystal planes, J. Catal. 229 (2005) 206–212.
[20] L. Gonzalez-Rovira, J.M. Sanchez-Amaya, M. Lopez-Haro, E. del Rio, A.B. Hungria, P. Midgley, J.J. Calvino, S. Bernal, F.J. Botana, Single-step process to prepare CeO_2 nanotubes with improved catalytic activity, Nano Lett. 9 (2009) 1395–1400.
[21] G.Z. Chen, C.X. Xu, X.Y. Song, W. Zhao, Y. Ding, S.X. Sun, Interface reaction route to two different kinds of CeO_2 nanotubes, Inorg. Chem. 47 (2008) 723–728.
[22] T. Taniguchi, K. Katsumata, S. Omata, K. Okada, N. Matsushita, Tuning growth modes of ceria-based nanocubes by a hydrothermal method, Cryst. Growth Des. 11 (2011) 3754–3760.
[23] T. Naganuma, E. Traversa, Stability of the Ce(3+) valence state in cerium oxide nanoparticle layers, Nanoscale 4 (2012) 4950–4953.
[24] A.I.Y. Tok, S.W. Du, F.Y.C. Boey, W.K. Chong, Hydrothermal synthesis and characterization of rare earth doped ceria nanoparticles, Mater. Sci. Eng. A: Struct. Mater. Prop. Microstruct. Process. 466 (2007) 223–229.
[25] Q. Wu, F. Zhang, P. Xiao, H.S. Tao, X.Z. Wang, Z. Hu, Y.N. Lu, Great influence of anions for controllable synthesis of CeO_2 nanostructures: from nanorods to nanocubes, J. Phys. Chem. C 112 (2008) 17076–17080.
[26] M. Hirano, E. Kato, Hydrothermal synthesis of nanocrystalline cerium(IV) oxide powders, J. Am. Ceram. Soc. 82 (1999) 786–788.
[27] B. Acosta, E. Smolentseva, S. Beloshapkin, R. Rangel, M. Estrada, S. Fuentes, A. Simakov, Gold supported on ceria nanoparticles and nanotubes, Appl. Catal. A: Gen. 449 (2012) 96–104.
[28] A. Galtayries, R. Sporken, J. Riga, G. Blanchard, R. Caudano, XPS comparative study of ceria/zirconia mixed oxides: powders and thin film characterisation, J. Electron Spectrosc. Relat. Phenom. 88 (1998) 951–956.
[29] Z.L. Wu, M.J. Li, J. Howe, H.M. Meyer, S.H. Overbury, Probing defect sites on CeO_2 nanocrystals with well-defined surface planes by Raman spectroscopy and O-2 adsorption, Langmuir 26 (2010) 16595–16606.
[30] W.H. Weber, K.C. Hass, J.R. McBride, Raman-study of CeO_2-2nd-order scattering, lattice-dynamics, and particle-size effects, Phys. Rev. B 48 (1993) 178–185.
[31] B. Solsona, T. Garcia, R. Murillo, A.M. Mastral, E.N. Ndifor, C.E. Hetrick, M.D. Amiridis, S.H. Taylor, Ceria and gold/ceria catalysts for the abatement of polycyclic aromatic hydrocarbons: an in situ DRIFTS study, Top. Catal. 52 (2009) 492–500.
[32] C. Binet, M. Daturi, J.C. Lavalley, IR study of polycrystalline ceria properties in oxidised and reduced states, Catal. Today 50 (1999) 207–225.
[33] S. Deshpande, S. Patil, S. Kuchibhatla, S. Seal, Size dependency variation in lattice parameter and valency states in nanocrystalline cerium oxide, Appl. Phys. Lett. 87 (2005) 3.